Journal of ELECTRONIC MATERIALS, Vol. 38, No. 12, 2009
DOI: 10.1007/s11664-009-0849-5
© 2009 TMS
Special Issue Paper

Multiphase Field Simulations of Intermetallic Compound Growth During Lead-Free Soldering

M.S. PARK[1] and R. ARRÓYAVE[1,2]

1.—Department of Mechanical Engineering, Texas A&M University, College Station, TX 77840, USA. 2.—e-mail: rarroyave@tamu.edu

A multiphase field simulation of the morphological evolution of the intermetallic compounds (IMCs) formed during the reaction between liquid Sn-based solder and a copper substrate is presented. The Cu-substrate, Cu_3Sn (ϵ phase), and Cu_6Sn_5 (η phase) layers (or grains), as well as the Sn-liquid phase are considered. Interfaces are defined by the presence of more than one phase at a given point of the computational domain. The interface structure is determined by assuming that all components of coexisting phases within the interfacial region have equal chemical potentials, which are in turn calculated from CALPHAD thermodynamic databases. Fast grain boundary (GB) diffusion in the η IMC layer, η grain coarsening and growth with growth/shrinkage of ϵ grains, and dissolution of Cu from the substrate will be discussed and compared with previous works. The simulation will address the kinetics of the IMC growth during soldering and the influence of fast GB diffusion on the concurrent coarsening of Cu_3Sn and Cu_6Sn_5 grains. The kinetic behavior of the substrate/IMC/solder system as a function of model parameters will also be presented.

Key words: Multiphase field model, morphology, lead-free soldering, intermetallic compound growth, Cu_6Sn_5, Cu_3Sn

INTRODUCTION

During soldering, interfacial interactions with the substrate result in the formation and growth of complex intermetallic (IMC) phases at the substrate/solder interface. In general, the IMC reaction consists of several complex processes. At first, the substrate partially dissolves into the molten solder alloy once they come into contact. Close to the substrate/solder interface, the liquid becomes supersaturated with the dissolved metal. This supersaturation leads to the eventual precipitation and subsequent growth of intermetallic compounds. This stage is critical for the evolution of the IMCs, in that initial intermetallic compound growth and interfacial morphology determine in great measure the reliability of soldered assemblies obtained through a given soldering process. The nature of the interfacial reactions depends on the individual alloy systems and soldering temperatures under consideration.[1–7] In Cu-Sn/Cu systems, the intermetallic layers typically formed at the substrate/solder interface at the early stages of the soldering process have been observed to consist mostly of Cu_6Sn_5, with Cu_3Sn being a minor constituent of the IMC layer. It is important to note that, at later stages, Cu_3Sn can become the dominant constituent of the IMC layer, depending on the particular soldering conditions and the relative amounts of the reactants (Cu and Sn). Understanding the solder/substrate interactions and their microstructural evolution at the interface is important as it can provide insight into the nature of the interfacial evolution from a metallurgical point of view.[8–13] At the same time, accurate control of these reactions can have significant impact on the optimization of the soldering process.[14]

Experimental investigations of intermetallic compound growth[6,7,13,15–18] indicate that Cu_6Sn_5 layer is formed as scallop-type grains in contact with liquid solder, while Cu_3Sn is usually formed

(Received February 27, 2009; accepted May 18, 2009; published online June 16, 2009)

between the Cu substrate and the Cu_6Sn_5 layer. Although the stability and morphology of IMC layers formed during the soldering reactions have been extensively studied, there remain significant questions on how the different microstructural and material factors (grain boundary and interfacial structure, short-circuit diffusion paths, surface and interfacial energies) determine the interfacial structure observed under particular soldering conditions. Through the use of simplified computational models, it is possible to address some of these questions. These models, coupled with critical experiments, can in turn be used to design better soldering practices.

Accurate knowledge of the thermodynamic behavior of the constituents of a given reacting (i.e., substrate/solder) material system provides fundamental information necessary to analyze the different possible reactions between system constituents, determine the stabilities of different phases, as well as predict the driving forces for chemical reactions and diffusion processes.[19] However, knowledge of the equilibrium state of the system is not sufficient to understand the complex microstructural phenomena occurring as the solder interacts with the substrate. The particular path that the system takes as it approaches equilibrium depends on the local minimization of the system's total free energy, which in turn is determined not only by the local composition but also by the presence of free surfaces and interfaces, as well as by nonlocal contributions. It is thus necessary to describe the time evolution behavior of the substrate/solder interface. Recently, it has been shown that phase field approaches[20,21] can be used to simulate soldering reactions,[22,23] which in turn provides us with a powerful tool to describe the complex microstructural evolution of intermetallic compounds in which significant topological changes in the microstructure take place as the reaction progresses.

In this study, we will briefly introduce the development of a phase field model[20] based on the previous work by Huh and Hong[23] to be used in the simulation of the microstructural evolution of the IMC layer formed by the interfacial reactions in the Cu-Sn system at 523 K. We will show different morphologies of IMC layer during soldering reaction with changing material parameters in the presence of Cu_6Sn_5 and Cu_3Sn. The phase field simulations account for the fast grain boundary diffusion in the IMC layer and grain coarsening by using different grain boundary diffusion coefficients, for concurrent coarsening of the IMC grains by using different solder/IMC interfacial energies, and for dissolution from the substrate and intermetallic compound layer by using different initial liquid solder compositions. They include the different kinetics of the IMC layer formed by the soldering reaction between the liquid solder and the substrate in the presence of Cu_6Sn_5 and Cu_3Sn.

PHASE FIELD AND DIFFUSION EQUATIONS

We consider a Cu-Sn binary system at 523 K. The system is composed of a Sn-rich liquid solder (L), a Cu-rich solid substrate (α), an intermetallic compound layer of Cu_6Sn_5 (η), and an intermetallic compound layer of Cu_3Sn (ε). The IMC layers form between the liquid solder and the Cu substrate, and the η-IMC lies on the ε-IMC.

The IMC layers consist of many grains that are differentiated by nonconserved phase fields.[18] The spatial distribution of the liquid solder, the substrate, and the grains in the intermetallic layer of the system is mathematically expressed by using N arrays of phase fields $\phi_i(x,t)$ (i = 1,…, N), which can be expressed with multiphase field variables. The phase field variables in this model can be defined as ϕ_1 for solid substrate, $\phi_{2,\ldots,N-1}$ for the grains in the two IMC layers, and ϕ_N for liquid solder. $\phi_i = 1$ indicates that phase i exists at that point of space, while $\phi_i = 0$ indicates that i phase does not exist in the region. Additionally, interfaces are defined in the system whenever $0 < \phi_i < 1$. Within the interface, ϕ_i is considered to change continuously within the range $0 < \phi_i < 1$; for example, if $0 < \phi_1 < 1$ and $0 < \phi_2 < 1$ at a point in an interface region, the point indicates the presence of the η-IMC layer and a solid substrate. In the same way, we can expect phase information at any point from phase field variables. From previous works,[20,24,25] the interface is considered as a finite region of a mixture of different phases (or grains) so that the phase field variables at any position in the system are subject to the following constraints:

$$\sum_{i=1}^{N} \phi_i = 1 \tag{1}$$

and

$$c(x,t) = \sum_{i=1}^{N} \phi_i c_i. \tag{2}$$

The free energy density f can be defined as follows:

$$f = \sum_{j>i} \sum_{i} \left[-\frac{\epsilon_{ij}^2}{2} \nabla\phi_i \cdot \nabla\phi_j + \omega_{ij}\phi_i\phi_j \right] + \sum_{i} \phi_i f^i(c_i), \tag{3}$$

so that the total free energy functional with respect to system volume can be defined[20,21] as

$$F = \int_V \left[\sum_{j>i} \sum_{i} \left[-\frac{\epsilon_{ij}^2}{2} \nabla\phi_i \cdot \nabla\phi_j + \omega_{ij}\phi_i\phi_j \right] + \sum_{i} \phi_i f^i(c_i) \right] \mathrm{d}V, \tag{4}$$

where f^i is the chemical free energy density of phase i and depends on the phase composition c_i. ϵ_{ij} is the gradient energy coefficient, which is related to the energy penalty involved in forming an interface, and ω_{ij} is a double-well potential representing the energy barrier between two phases i and j. The advantage of using the double-well potential is that it allows the temporal evolution of the phase fields to be computed for a finite region of the interface.

At any point in the interface, compositions can be determined by Eq. 2 and assuming a condition of local thermodynamic equilibrium,[25] which can be defined as

$$f^1_{c_1}[c_1] = f^2_{c_2}[c_2] = f^3_{c_3} \cdot [c_3] = \ldots = f^N_{c_N}[c_N]. \qquad (5)$$

This equilibrium allows continuity in the chemical potential of all the species across the interfaces. Elimination of the extra chemical potential in turn relaxes the restrictions on the width of the numerical interfaces during the simulations.[20]

The number of phases coexisting at a given point can be obtained as[20]

$$N_\mathrm{p}(x,t) = \sum_i^N \chi_i(x,t). \qquad (6)$$

According to the consideration of a phase field description for coexisting phases at interfaces, we can obtain the evolution of the phase field as a function of time[21] as

$$\frac{\partial \phi_i}{\partial t} = -\frac{2}{N_\mathrm{p}} \sum_{i \neq j} \chi_i \chi_j M_{ij} \left[\frac{\partial F}{\partial \phi_i} - \frac{\partial F}{\partial \phi_j} \right], \qquad (7)$$

where χ_i is equal to 1 when the corresponding phase exists and is 0 otherwise, and N_p represents the number of the coexisting phases at a calculated position. This equation is only valid on the phase interfaces since the presence of only one phase in any point of the calculation domain renders χ_i or χ_j equal to 0. M_{ij} represents the mobility of the interfacial region. The derivative of the free energy functional $\partial F/\partial \phi_i$ is given by

$$\frac{\partial F}{\partial \phi_i} = \sum_{i \neq j} \left[\frac{\epsilon_{ij}^2}{2} \nabla^2 \phi_j + \omega_{ij} \phi_j \right] + f^i(c_i) - f_c c_i. \qquad (8)$$

For a diffusion equation, we set the flux equation with respect to the diffusion coefficient, free energy density, and composition gradient for the multiphase system. The flux equation can be modified into a diffusion equation by using spatial differentiation with diffusivity that varies as a function of the (nonconserved) phase field variables. The diffusion equation can be obtained as

$$\frac{\partial c}{\partial t} = \nabla \cdot \left(D(\phi_i) \sum_{i=1}^N \phi_i \nabla c_i \right). \qquad (9)$$

In order to get model parameters in the multiphase field equation, we should obtain a stationary solution of the phase field equation in a planar interface. The solution can then be associated with interfacial energy and interfacial width. According to the definition of the interface energy as a function of gradient energy coefficient and phase field with a referred interface width, we can obtain two relationships between model parameters and material parameters, as previously shown:[21,23]

$$\epsilon_{ij} = \frac{4\sqrt{\xi \sigma_{ij}}}{\pi} \quad \text{and} \quad \omega_{ij} = \frac{2\sigma_{ij}}{\xi}, \qquad (10)$$

where ξ is a half of the width of the interface, and σ_{ij} is the interface energy for the corresponding phases. Based on the approximation of the interface thickness,[25] ξ has a fixed value.

Numerical Implementation

The multiphase field equation and the diffusion equation were solved numerically by using the finite-difference method on the cross-section of the Cu/Sn solder joint at 523 K in two spatial dimensions. In all cases, the values of the dimensional grid spacing h (=Δx) and the half-width of the interface ξ used were 1.0×10^{-8} m and $4h$, respectively. It is important to note that in this work we neglect the treatment of nucleation at the substrate/solder interface. Although this in principle can be tackled either through thermal noise or by applying classical nucleation theory, this component of the problem is outside the scope of the present work.

Figure 1 shows a schematic configuration for the computational domain. The size of the system is set to be $158h \times 101h$. The Cu substrate, ε-IMC layer, η-IMC layer, and liquid solder layer are positioned from bottom to top in the initial array of phases.

The η-IMC layer is four or five times thicker than the ε-IMC layer in height and a grain in the η phase is four or five times wider than a grain in the ε phase.[18] The ε- and η-IMC layers are placed from $21h$ to $26h$ and from $27h$ to $41h$, respectively, between the liquid solder (from $42h$ to $101h$) and the solid substrate (from $0h$ to $20h$). The η-IMC layer initially consists of 12 rectangular grains that have different widths between $10h$ and $15h$, and the ε-IMC layer initially consists of 34 rectangular grains that have different widths between $5h$ and $6h$ (Fig. 1). Periodic boundary conditions are applied to the sides of the calculation domain and Neumann boundary conditions are applied to the top and bottom of the calculation domain. The calculations are finished when the thickness of the Cu substrate is arbitrarily close to zero.

The free energy densities per unit molar volume of individual phases can be obtained from the CALPHAD method[26] and are listed in the Appendix. We assumed that all phases have the same molar volume (v_m = 16.29 cm^3/mole), and f_η is formulated

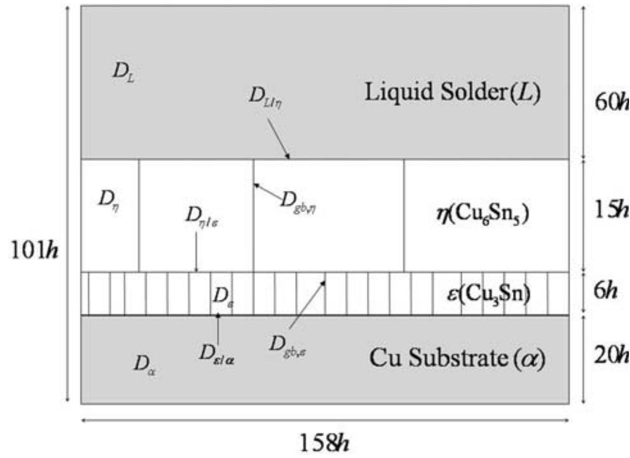

Fig. 1. Schematic configuration for the computational domain.

as a parabolic function in order to allow a limited solubility range in the η phase. The equilibrium phase compositions can be solved by using Eqs. 12–15. They are

$$\begin{aligned} c_\alpha^{\alpha\varepsilon} &= 0.027, \quad c_\varepsilon^{\varepsilon\alpha} = 0.227, \quad c_\eta^{\eta\varepsilon} = 0.433, \\ c_\varepsilon^{\varepsilon\eta} &= 0.247, \quad c_\eta^{\eta L} = 0.436, \quad c_L^{L\eta} = 0.977, \end{aligned} \tag{11}$$

where $c_\alpha^{\alpha\varepsilon}$ is the equilibrium composition of the α phase at the α–ε interface, and the other terms are defined correspondingly. The initial compositions of the substrate and ε and η intermetallic compound layers are taken to be uniform as $c_\alpha = 0.002$, $c_\varepsilon = 0.237$, and $c_\eta = 0.435$, respectively. The initial composition of the liquid solder phase is chosen to be either $c_L = c_L^{L\eta}$ corresponding to a Cu-saturated solder, or $c_L = c_L^{L\eta} + 0.02$, corresponding to a nearly pure Sn solder.

Determination of material parameters used in the simulation is very difficult because material properties of single phases, for example, the material parameters for the α, η, ε, and L phases in this study (surface, interfacial energies and mobilities, etc.), are dependent on the theoretical approach used to examine experimental data.[6,16,27–29] Determination of material properties at the interfaces is even more difficult because these structures are model artifacts and thus do not have a physical meaning.

The diffusivities and other material parameters employed in the numerical calculation are summarized as following: diffusion coefficients of the liquid solder (L), the IMC layers (η and ε), and Cu substrate (α) are $D_L = 2.0 \times 10^{-12}$ m^2/s, $D_\eta = 8.0 \times 10^{-17}$ m^2/s, $D_\varepsilon = 4.0 \times 10^{-18}$ m^2/s, and $D_\alpha = 8.0 \times 10^{-19}$ m^2/s, respectively. Diffusion coefficients of interfaces are $D_{\eta L} = 4.0 \times 10^{-13} D_L$ (m^2/s), $D_{\varepsilon\alpha} = 2.0 \times 10^{-16}$ m^2/s, $D_{\eta\varepsilon} = 2.0 \times 10^{-16}$ m^2/s, $D_{\eta\eta} = 4.0 \times 10^{-14}$ m^2/s, and $D_{\varepsilon\varepsilon} = 4.0 \times 10^{-16}$ m^2/s. The interfacial energies are taken as $\sigma_{\eta L} = 0.1$ J/m^2 and $\sigma_{\alpha\varepsilon} = \sigma_{\alpha\eta} = \sigma_{\eta\eta} = \sigma_{\varepsilon\varepsilon} = 0.3$ J/m^2. Mobilities are taken as $M_{\eta L} = 1.0 \times 10^{-6}$ m^2/s and $M_{\alpha\varepsilon} = M_{\eta\varepsilon} = M_{\varepsilon\varepsilon} = M_{\eta\eta} = 7.0 \times 10^{-8}$ m^2/s.

It is important to note that critical parameters for the simulation listed above, such as interfacial energies and mobilities are notoriously difficult to determine experimentally let alone computationally, and are thus used as simulation parameters which only carry a physical meaning when viewed as normalized quantities.

RESULTS AND DISCUSSIONS

The simulation in this study will follow the morphology of IMC grain growth as it is affected by the different material properties and model parameters, such as the diffusion coefficient of grain boundary, the interfacial energy between η-IMC layer and liquid solder, as well as the initial Cu content in the liquid solder.

In order to examine how the kinetics of η-IMC growth is affected by grain boundary diffusion, simulations were carried out with three different grain boundary diffusion coefficients. The first is a high diffusion coefficient of $D_{\eta\eta} = 4.0 \times 10^{-14}$ m^2/s, indicating that more mass is likely to diffuse through the grain boundaries than through the grains. The second is an intermediate diffusion coefficient of $D_{\eta\eta} = 4.0 \times 10^{-15}$ m^2/s, which can be obtained from interdiffusion formulations. The last is a low diffusion coefficient of $D_{\eta\eta} = D_\eta$, indicating that the mass diffusion rate through grain boundaries is the same as that through grains. For all three cases, the initial solder composition is set to $c_L = c_L^{L\eta}$ and the L–η interfacial energy is taken to be the value quoted in the previous section.

Figure 2 shows the intermetallic compound growth for the three cases of different grain boundary diffusion at $t = 20$ s. As the intermetallic compound layer grows thicker with time, there is concurrent coarsening of the η and ε grains, resulting in fewer grains remaining in the intermetallic compound layer. While the number of grains that have survived in both layers is similar, the relative thickness of the ε-IMC and η-IMC layers varies according to the different grain boundary diffusion, as shown in Fig. 3. We can see that η–L and ε–η interfaces have opposite signs of curvature, resulting in the scallop shape for η grains and the thin-film shape for ε grains as already observed.[18,23]

In the case of high grain boundary diffusion, we can see that the thickness of the η-IMC layer increases at a faster rate than in the other cases, while that of the ε-IMC layer decreases. Reduction of the Cu substrate thickness occurs at the same rate regardless of the different grain boundary diffusion rates. Precisely speaking, the thickness of the ε-IMC layer increases but the η–ε interface moves down faster than the α–ε interface, resulting in encroachment of the η-IMC phase into the ε-IMC layer. Due to the high grain boundary diffusion, an increase in the flux of Sn from the liquid solder, through the grain boundary, and into the IMC layers is expected. When Sn flows through the grain

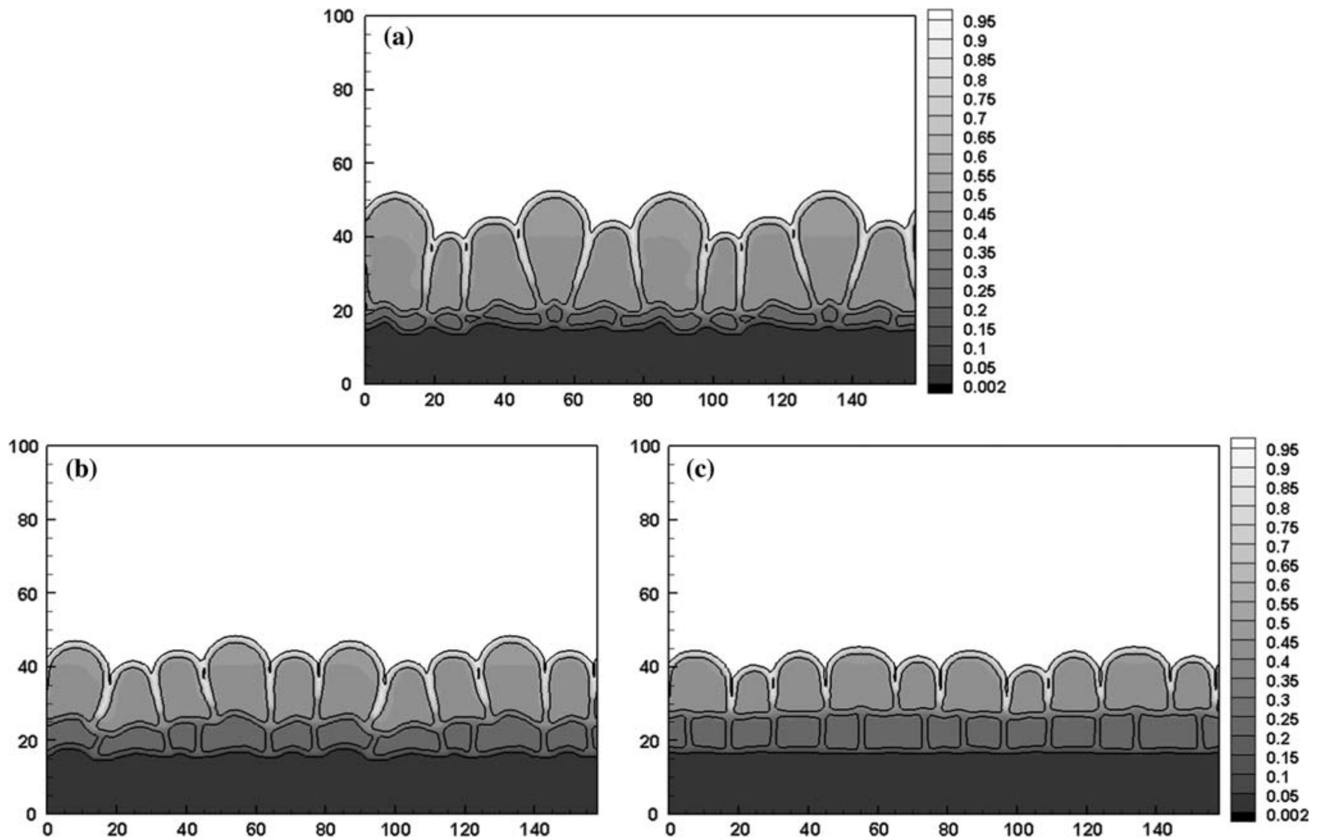

Fig. 2. Microstructural evolution of the intermetallic compound layer for the cases: (a) high grain boundary diffusion ($D_{\eta\eta}$ = 4.0 × 10^{-14} m^2/s), (b) intermediate grain boundary diffusion ($D_{\eta\eta}$ = 4.0 × 10^{-15} m^2/s), and (c) low grain boundary diffusion ($D_{\eta\eta}$ = 8.0 × 10^{-17} m^2/s) at t = 20 s.

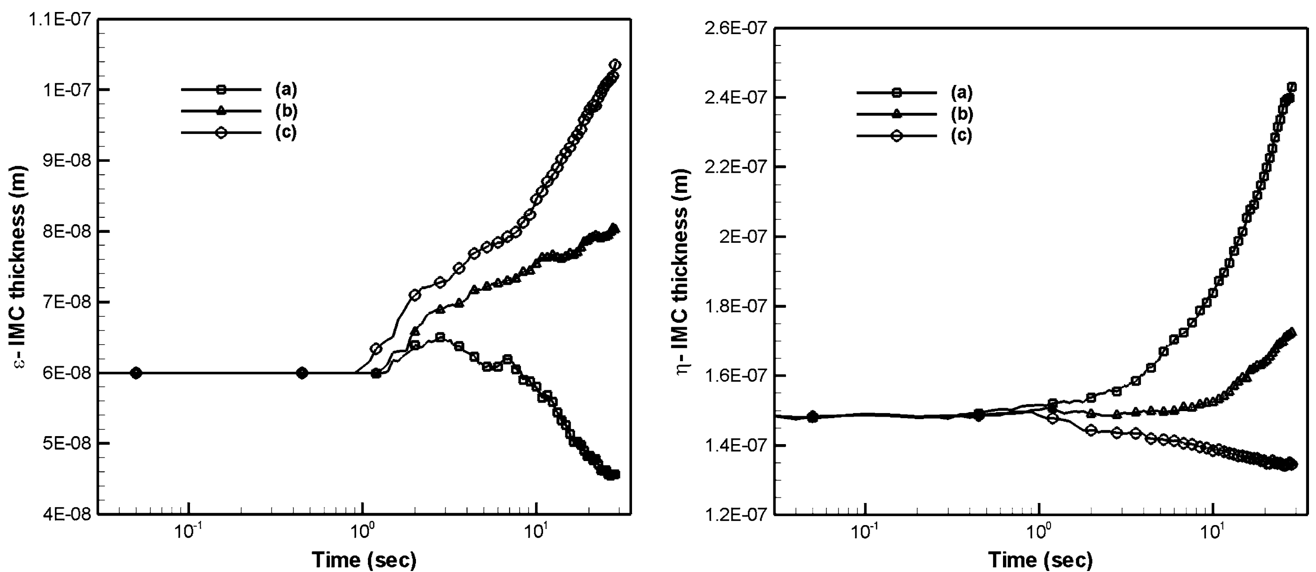

Fig. 3. Evolution of ε-IMC layer and η-IMC layer thickness with respect to time, corresponding Fig. 2a–c.

boundary of the η-IMC layer to form η-IMC and ε-IMC, both the η-IMC and ε-IMC layers simultaneously increase. However, excess Sn flux at the η–ε interface results in conversion of Cu_3Sn to Cu_6Sn_5 because Cu_6Sn_5 is the most stable product of the chemical reaction in the Cu-Sn system under those conditions. It is important to note that this encroachment behavior has been observed in many

experimental investigations[3,30,31] and has already been explained by using the additional chemical reaction between η-IMC and ε-IMC.[32]

In the case of intermediate grain boundary diffusion, we can expect that there is a high probability that Sn diffuses from the liquid solder through the grain boundaries, resulting in simultaneous growth of η-IMC and ε-IMC. This means that there is no more extra Sn supply from the liquid solder for the reactive phase transformation from ε-IMC to η-IMC. The growth speed of η-IMC in Fig. 3b is likely to be less than that in Fig. 3a because no encroachment is observed.

When the grain boundary diffusion is the same as that for the grains in the η layer, we can see that the thickness of the η-IMC layer decreases while that of the ε-IMC layer increases. A decrease in the supply of Sn to the IMC layer results in the growth of Cu_3Sn at the expense of Cu_6Sn_5. This stabilization of Cu_3Sn due to depletion of Sn has already been observed experimentally.[33]

The concurrent coarsening of the η grains on the IMC layer growth in calculations are carried out by changing the η–L interfacial energy as shown in Fig. 4a ($\sigma_{\eta L}$ = 0.05 J/m^2) and Fig. 4b ($\sigma_{\eta L}$ = 0.15 J/m^2). Other material parameters for Fig. 4 are adopted from the case of Fig. 3a.

Although high grain boundary diffusion is employed in the η phase, there is a smaller tendency for competitive grain growth at the η–L interface compared with the case shown in Fig. 3a because of the lower value of $\sigma_{\eta L}$. The coarsening rate is related to the grain boundary diffusion and difference between $\sigma_{\eta L}$ and $\sigma_{\eta\eta}$.[23] In this case, while the high grain boundary diffusion contributes to an increase in the rate of grain growth, the higher difference between the two interfacial energies leads to grain boundary wetting, which essentially pins the η–L interfaces, thus limiting lateral growth of the η grains. Therefore, the grains grow upward with less coarsening with neighboring grains in η-IMC layer. The growth rate in this case is observed to be faster than the case shown in Fig. 3a due to the fact that most of the short-circuit diffusion is through the liquid layer in between η grains, which is even faster than the solid-state grain boundary diffusion. Due to the increased Sn flux, encroachment of the ε-IMC layer in Fig. 4a occurs faster than for the case shown in Fig. 3a. On the other hand, if relatively higher interfacial energy is applied at the η–L interface, the reversed behavior of grain growth can be expected. This means that high $\sigma_{\eta L}$ stimulates faster spreading of a grain and faster coarsening with neighboring grains, resulting in less upward grain growth and fewer grains that survive at any given time. Less Sn flux caused by reduced fast diffusion paths causes a slight increase of the ε-IMC layer because of the phenomena already discussed with regard to Fig. 3c. High Cu consumption can be expected in the case of low interfacial energy because Cu consumption is affected by the total thickness of the two IMC layers. All explanations for morphologies of IMC development is accompanied by Fig. 5

Microstructural evolution of the IMC was also simulated based on an initial solder composition changed from pure Sn liquid solder ($c_L = c_L^{L\eta} + 0.02$) as shown in Fig. 6a and Cu-supersaturated liquid solder ($c_L = c_L^{L\eta} - 0.02$) as shown in Fig. 6b. Liquid solder composition far from the IMC layers and the two IMC layer thicknesses with respect to time are shown in Fig. 7.

Since the initial liquid solder is set to be pure Sn in Fig. 6a, dissolution of Cu from the η-IMC layer and Cu substrate occurs at the early stages of soldering. Because of the dissolution of Cu from the η-IMC layer into liquid solder (caused by liquid solubility), the η-IMC layer shrinks at the η–L interface quickly, which causes faster grain coarsening. After shrinkage of the η-IMC layer with fewer surviving grains, we can expect that the liquid solder composition becomes Cu enriched, that the dissolution rate of Cu from the intermetallic compound layer and Cu substrate decreases, and

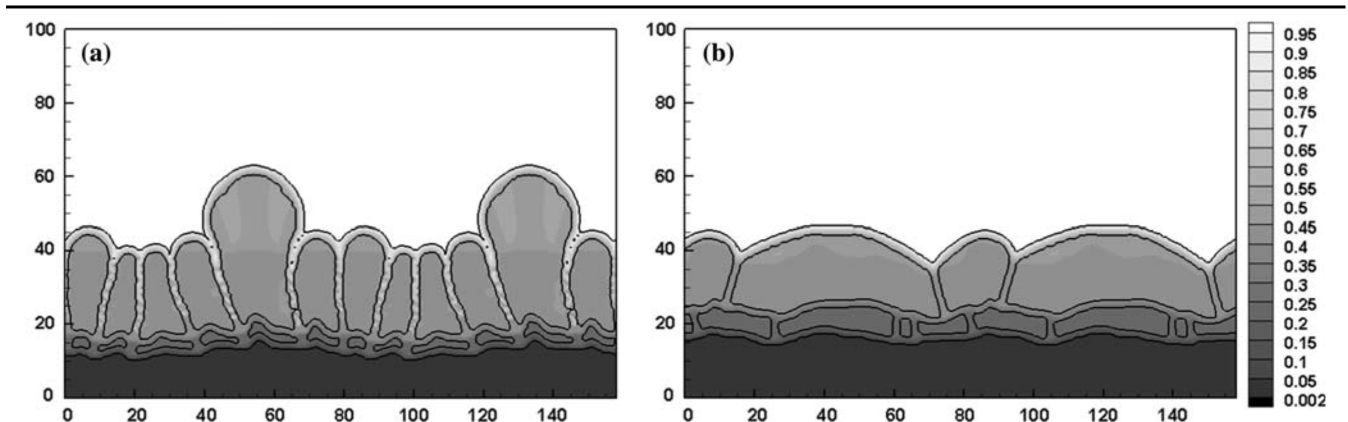

Fig. 4. Microstructural evolution of the IMC layer for the case of (a) the low η–L interfacial energy ($\sigma_{\eta L}$ = 0.05 J/m^2) and (b) high η–L interfacial energy ($\sigma_{\eta L}$ = 0.15 J/m^2) at t = 20 s.

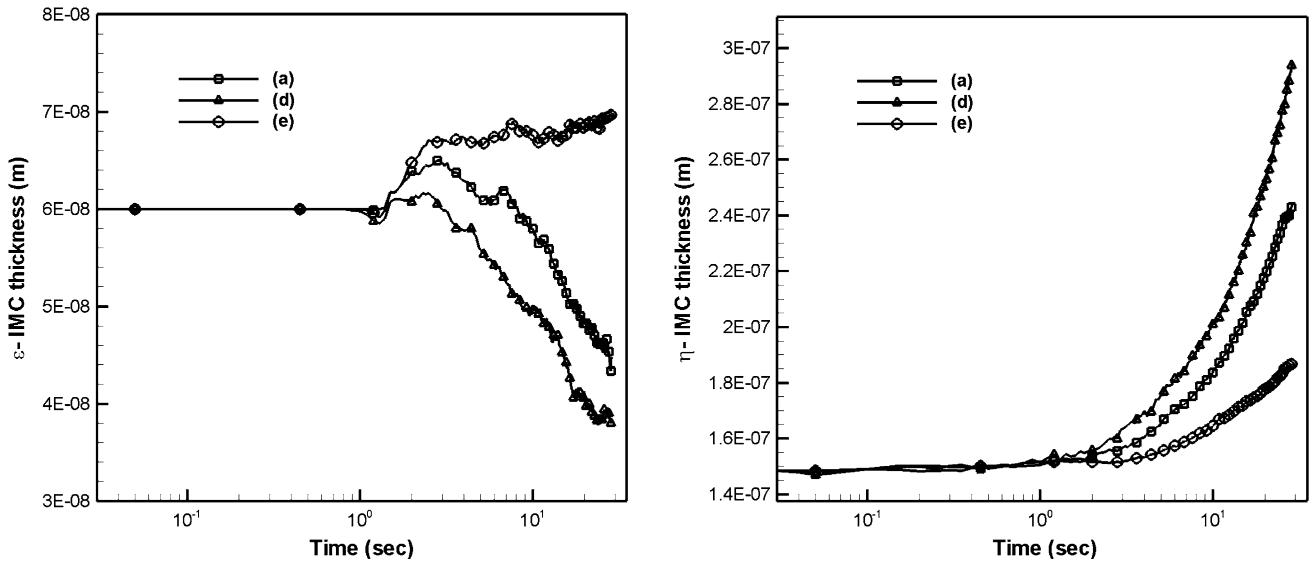

Fig. 5. Evolution of the thickness of the two IMC layers with respect to time for Fig. 4a and b compared with Fig. 3a.

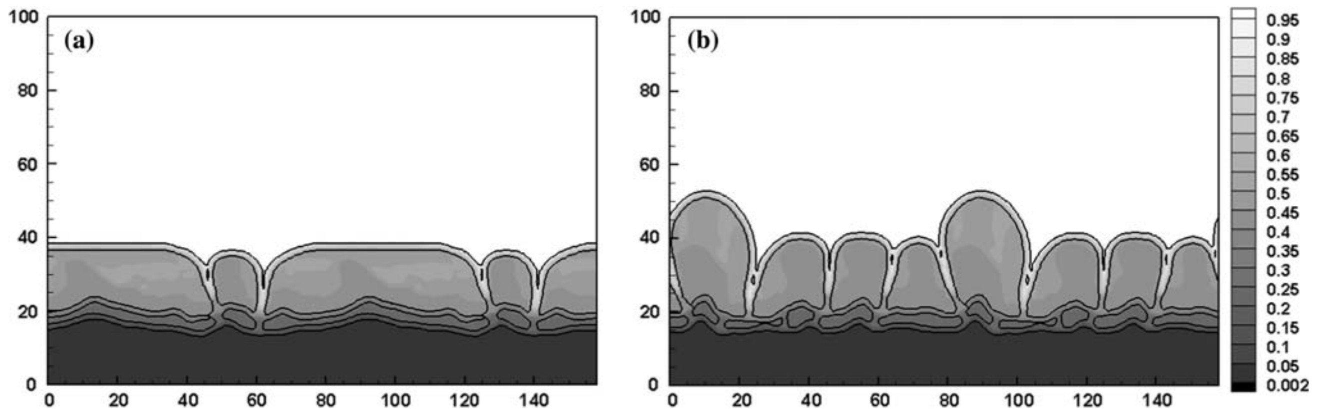

Fig. 6. Microstructural evolution of the IMC layer for the case of (a) pure Sn liquid solder ($c_L = c_L^{L\eta} + 0.02$) and (b) Cu-supersaturated liquid solder ($c_L = c_L^{L\eta} - 0.02$) at $t = 20$ s.

that the η-IMC layer thickness starts to grow at the $\eta{-}\varepsilon$ interface due to the encroachment behavior. From the point of view of the ε-IMC layer, its thickness decreases due to suppression at an early stage as well as encroachment from the η-IMC layer at the late stage.

When the initial liquid solder is set to be supersaturated with Cu, the composition of the liquid solder is likely to approach the equilibrium composition according to liquid solubility. In order to reach this equilibrium composition, liquid solder requires more Sn from all phases, which causes a slight excess of Sn flux on the liquid solder, but not more than in the case of the pure Sn liquid solder. After excess of Sn flux diffuse into the liquid solder area, the thickness change of the two IMC layers during the soldering reaction follows the same physics as the case shown in Fig. 3a.

CONCLUSIONS

The present work offers a relatively simple example of the application of sophisticated phase field modeling approaches in combination with CALPHAD thermodynamic models to investigate complex reactive phase formation phenomena. The model developed allows the investigation of the different factors that influence the relative thickness and grain morphology of IMC layers formed at the initial stages of the reaction between a Cu substrate and Sn solder alloy.

The morphological evolution and growth of the IMC (Cu_6Sn_5 and Cu_3Sn) layer during lead-free soldering with Sn-Cu solder alloys on a Cu substrate was performed using a multiphase field model. The multiphase field simulations were performed by using three different grain boundary diffusion

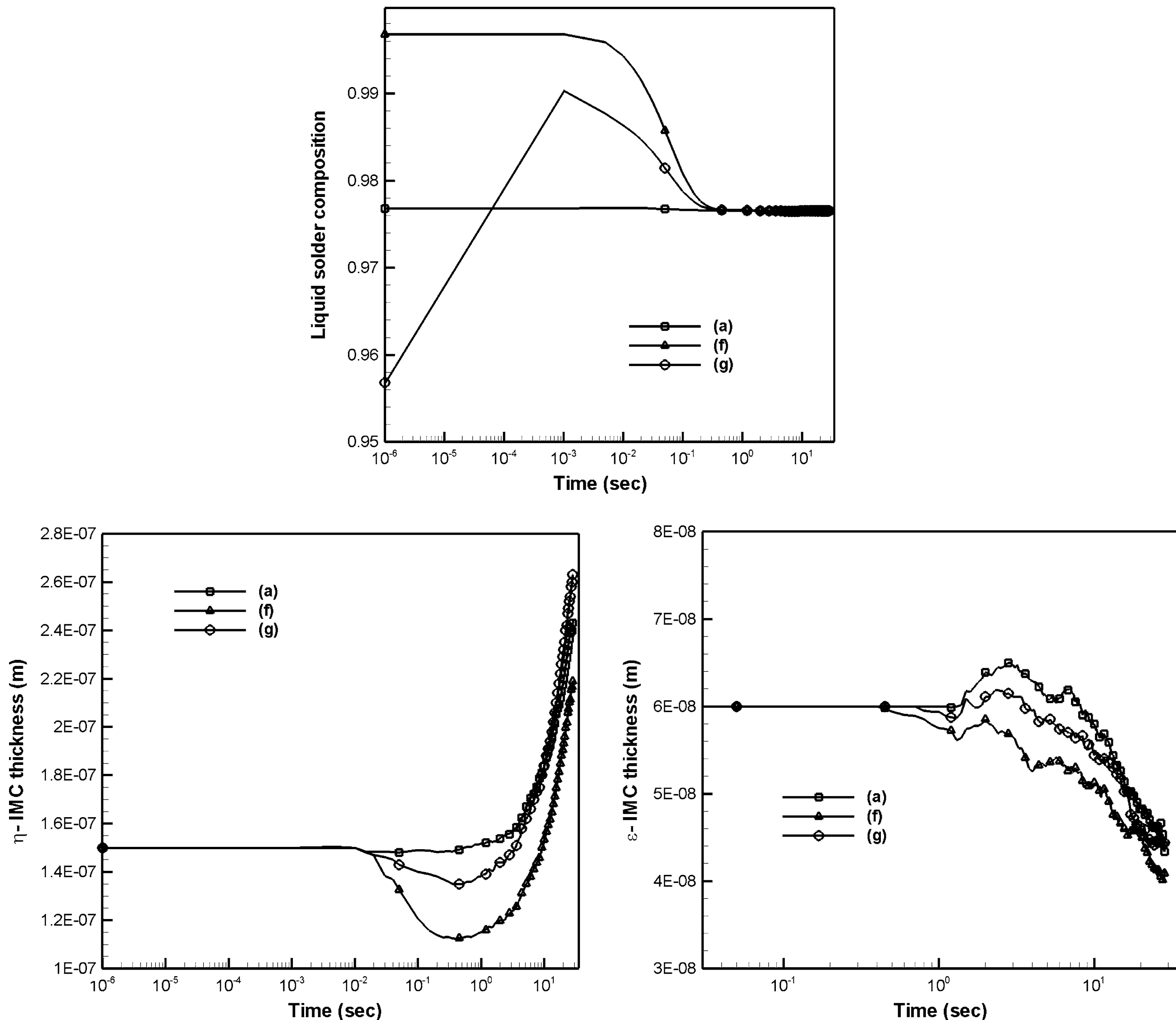

Fig. 7. Evolution of liquid solder composition far from the IMC layers in the case of Fig. 6a and b compared with Fig. 3a.

coefficients in the η-IMC layer, three different interfacial energies of η–L interface (causing concurrent coarsening of the IMC grains along with IMC layer growth), and three different initial liquid solder compositions (inducing dissolution of Cu from the Cu substrate and IMCs).

The microstructural evolution of the two IMC layers appeared more complicated compared with previous works.[22,23] However, it was found that by controlling three independent model parameters (grain boundary diffusion, η–L interfacial energy and initial liquid solder) it was possible to reproduce in a qualitative manner many previous experimental investigations of this system. Specifically, the simulations presented in this work allowed us to make the following observations: (i) high grain boundary diffusion leads to increase of the η-IMC layer thickness and decrease of the ε-IMC layer thickness; (ii) high η–L interfacial energy leads to a decrease of grain boundary wetting, resulting in an increase of grain coarsening; (iii) as a net result of the concurrent dissolution and growth of the η-IMC layers in the case of poor Sn liquid solder, the η-IMC layer thickness decreases at the early stages of soldering; and (iv) ε-IMC is affected by the behavior of the η-IMC layer and Sn flux from liquid solder.

ACKNOWLEDGEMENTS

The authors are grateful to Saurabh Bajaj and Arpita Chari for their help with the preparation of the manuscript. Most of the calculations were carried out on the CAT cluster of the Department of Chemical Engineering at Texas A&M university. This research was supported by the National Science Foundation under NSF Grant No. CMMI-0758298. Partial funds were also provided through the George Bush Presidential Library Foundation Travel Grant.

APPENDIX

The free energy densities per unit molar volume of individual phases can be obtained from the CALPHAD method[26] as

$$f_\alpha = (1-c)G^\alpha_{\mathrm{Cu}} + cG^\alpha_{\mathrm{Sn}} + RT[(1-c) \in (1-c) + c\ln c] + c(1-c)\left[L^\alpha_0 + L^\alpha_1(1-2c)\right], \quad (12)$$

$$f_\varepsilon = 2.0\times10^5(c-0.249)^2 + 0.75G^\alpha_{\mathrm{Cu}} + 0.25G^{\mathrm{SER}}_{\mathrm{Sn}} - 8194.2 - 0.2043T, \quad (13)$$

$$f_\eta = 2.0\times10^5(c-0.435)^2 + 0.545G^\alpha_{\mathrm{Cu}} + 0.455G^{\mathrm{SER}}_{\mathrm{Sn}} - 6869.5 - 0.1589T, \quad (14)$$

$$f_L = (1-c)G^L_{\mathrm{Cu}} + cG^L_{\mathrm{Sn}} + RT[(1-c)\ln(1-c) + c\ln c] + c(1-c)\left[L^L_0 + L^L_1(1-2c) + L^L_2(1-4c-4c^2)\right], \quad (15)$$

where

$$G^\alpha_{\mathrm{Cu}} = -19073.0,\ G^\alpha_{\mathrm{Sn}} = -27280.0,$$
$$G^{SER}_{\mathrm{Sn}} = 346160.0,\ G^L_{\mathrm{Cu}} = -11083.0,$$
$$G^L_{\mathrm{Sn}} = -28963.0,\ L^\alpha_0 = -11448.0,$$
$$L^\alpha_1 = -11694.0,\ L^L_0 = -10487.0,$$
$$L^L_1 = -18198.0,\ L^L_2 = 10528.4$$

REFERENCES

1. A.J. Sunwoo, J.W. Morris Jr., and G.K. Lucey Jr., *Metall. Trans. A* 23, 1323 (1992).
2. H.K. Kim and K.N. Tu, *Appl. Phys. Lett.* 67, 2002 (1995).
3. A.A. Liu, H.K. Kim, K.N. Tu, and P.A. Totta, *J. Appl. Phys.* 80, 2774 (1996).
4. S.K. Kang, R.S. Rai, and S. Purushothaman, *J. Electron. Mater.* 25, 1113 (1997).
5. C.H. Zhong and S. Yi, *Solder. Surf. Mount Tech.* 11, 44 (1999).
6. W.K. Choi and H.M. Lee, *J. Electron. Mater.* 29, 1207 (2000).
7. K.S. Kim, S.H. Huh, and K. Suganuma, *J. Alloy Compd.* 352, 226 (2003).
8. D.R. Frear and P.T. Vianco, *Metall. Mater. Trans. A* 25, 1509 (1994).
9. D. Yao and J.K. Shang, *Metall. Mater. Trans. A* 26, 2677 (1995).
10. M. Abtew and G. Selvaduray, *Mater. Sci. Eng. R* 27, 95 (2000).
11. C.K. Shin, Y.J. Baik, and J.Y. Huh, *J. Electron. Mater.* 30, 1323 (2001).
12. K.N. Tu and K. Zeng, *Mater. Sci. Eng. R* 27, 1 (2001).
13. P.L. Tu, Y.C. Chan, K.C. Hung, and J.K.L. Lai, *Scripta Mater.* 44, 317 (2001).
14. S. Bader, W. Gust, and H. Hieber, *Acta Metall. Mater.* 43, 329 (1995).
15. H.K. Kim, H.K. Liou, and K.N. Tu, *Appl. Phys. Lett.* 66, 2337 (1995).
16. H.K. Kim and K.N. Tu, *Phys. Rev. B* 53, 16027 (1996).
17. M. Schaefer, R.A. Fournelle, and J. Liang, *J. Electron. Mater.* 27, 1167 (1998).
18. J. Gorlich and G. Schmitza, *Appl. Phys. Lett.* 86, 053106 (2005).
19. K.K. Hong and J.Y. Huh, *J. Electron. Mater.* 35, 56 (2006).
20. I. Steinbach and F. Pezzolla, *Physica D* 134, 385 (1999).
21. S.G. Kim, W.T. Kim, T. Suzuki, and M. Ode, *J. Cryst. Growth* 261, 135 (2004).
22. M. Ode, T. Koyama, H. Onodera, and T. Suzuki, *J. Electron. Mater.* 32, 1534 (2003).
23. J.Y. Huh, K.K. Hong, Y.B. Kim, and K.T. Kim, *J. Electron. Mater.* 33, 1161 (2004).
24. S.G. Kim, W.T. Kim, and T. Suzuki, *Phys. Rev. E* 58, 3316 (1998).
25. S.G. Kim, W.T. Kim, and T. Suzuki, *Phys. Rev. E* 60, 7186 (1999).
26. J.H. Shim, C.S. Oh, B.J. Lee, and D.N. Lee, *Z. Metallkd.* 87, 205 (1996).
27. M. Onishi and H. Fujibuchi, *Trans. JIM* 16, 539 (1975).
28. Z. Mei, J.W. Sunwoo, and A.J. Morris Jr., *Metall. Trans. A* 23, 857 (1992).
29. Y.G. Lee and J.G. Duh, *J. Mater. Sci.* 33, 5567 (1998).
30. Y. Wu, J.A. Sees, C. Pouraghabagher, L. Foster, E.G. Jacobs, and R.F. Pinizzotto, *J. Electron. Mater.* 7, 769 (1993).
31. J. Lin and J. Jang, *Chapter 7 in Lead-free Electronics* (NY: Wiley, 2006), p. 383.
32. A.A. Liu,, K.N. Tu, T.T. Sheng, C.H. Tung, D.R. Frear, and P. Elenius, *J. Appl. Phys.* 87, 750 (2000).
33. J.Y. Song, J. Yu, and T.Y. Lee, *Scripta Mater.* 51, 167 (2004).